INVESTIGATING CAUSAL INTERACTIONS IN THE HUMAN BRAIN

USING EEG AND FNIRS

by

BORZOU ALIPOURFARD

Presented to the Faculty of the Graduate School of

The University of Texas at Arlington in Partial Fulfillment

of the Requirements

for the Degree of

MASTER OF SCIENCE IN BIOMEDICAL ENGINEERING

THE UNIVERSITY OF TEXAS AT ARLINGTON

AUGUST 2016

Acknowledgements

Abstract

INVESTIGATING CAUSAL INTERACTIONS IN THE

HUMAN BRAIN

USING EEG AND fNIRS

Borzou Alipourfard, M.S.

The University of Texas at Arlington, 2016

Supervising Professor: Hanli Liu

It is necessary for distributed neural assemblies to work in collaboration to achieve the most elementary brain functions. Activities within segregated neural assemblies are integrated to process an incredibly diverse collection of cognitive tasks. Measures such as correlation, cross-correlation, coherence and phase delay make limited use of the information that is available with the advanced multichannel and multimodal recordings of the brain's activity. They can also give spurious and false results. Most importantly, these bivariate measures are not capable of describing the interaction among multiple neural assemblies and the effective connectivity among them. Through causality analysis, we can identify these interactions and describe how information is transmitted across multiple parts, and make evident the presence of feedbacks in the network.

In this thesis, using Granger's causality and direct transfer function, I studied the brain's connectivity map at resting state. The direct transfer function is a normalized measure that uses the notion of Granger's causality to determine how much each channel can be considered a source of information for another channel at a particular frequency. I found out that at resting state with the eyes open, sources of information at both the theta and the alpha frequency band are localized to the frontal region of the head. I also used a modified version of Granger's causality, applicable to mixed frequency data, to investigate if the brain's electrical activity measured through EEG is causal to its hemodynamic activity measured using fNIRs. Through this algorithm, I found no evidence of brain's electrical activity being causal to its hemodynamic activity. I also investigated the relation between the spontaneous occipital alpha rhythm and the brain's hemodynamic fluctuations. Although my results show that there is a significant correlation between the occipital alpha rhythm and the hemodynamic fluctuations at the electrode sites F8 and F7, causality analysis did not reveal any causal influence from the alpha rhythm to the hemodynamic activity.

Table of Contents

List of Illustrations

List of Tables

Chapter 1

Introduction to Connectivity in The Human Brain

It is necessary for distributed neural assemblies to work in collaboration to achieve the most elementary brain functions. Activities within segregated neural assemblies are integrated to process an incredibly diverse collection of cognitive tasks. Evidence to the above claim is the distributed organization of our sensory system. Basic auditory, visual, and haptic cues are processed in parallel and in different areas of the cortex. They have to be integrated to represent the multimodal nature of our surrounding environment. A plethora of experimental evidence demonstrates this collaborative and synchronized activity across neural assemblies.

Neurons with related receptive fields in cat striate cortex show synchronized oscillation in response to visual stimuli [1]. This synchronization also occurs between neurons in the right and the left hemisphere and is mediated by corti-cortical connections [2]. Neuronal activity in areas of the visual and parietal cortex, and the parietal and motor cortex have also exhibited such synchrony [3]. More interestingly, it has been shown that selective attention mediates the evoked neural response, enhancing the auditory gamma-band transient response to auditory cues [4]. Abnormal patterns of synchrony have also been connected to pathological conditions. For patients with schizophrenia, significantly reduced phase synchrony in the beta band has been reported [5]. Other patterns of synchronized activity have been identified using cross-correlation and coherence analysis [6].

Measures such as correlation, cross-correlation, coherence and phase delay make limited use of the information that is available with the advanced multichannel and multimodal recordings of the brain's activity. They can also give spurious and false results. Significant phase delay and lagged correlation do not indicate the correct direction of information transfer or causality [7]. Coherence is subject to the artifacts arising from the volume conduction [8]. Most importantly, these bivariate measures are not capable of describing the interaction among multiple neural assemblies and the effective connectivity among them. Hence, they only provide a very limited and obscure picture of the actual underlying process and the connectivity structure [9].

Using Granger's causality to identify interactions among neural assemblies answers all of the difficulties mentioned above. It will show the correct direction of information transfer. It is not subject to artifacts due to volume conduction. Furthermore, it is a multivariate measure, and it can investigate the interactions among multiple channels simultaneously. It can describe how information is transmitted across multiple assemblies, and make evident the presence of feedback among them.

1.1 Granger's Causality

A times series, $Y(t)$, is Granger causal to another time series, $X(t)$, if and only if knowledge of the past of that time series, $Y(t - k), k = 1,2,3,..$, helps in predicting the present value of the other [7][10].

A mathematical formulation of this definition is helpful to elucidate the benefits and the advantages of using this measure. Consider a stationary mean zero time series $A(t)$ and let $A_p(t)$ represent the set of past values of $A(t)$:

$$A_p(t) = \{A(t-k): k = 1,2,\dots\}. \tag{1}$$

Let $U(t)$ be all the information in the universe accumulated until time $(t-1)$ and "$U(t)-A_p(t)$" to represent all this information apart from the past values of A. Define the optimum, unbiased, least-squares predictor of $A(t)$ using the set of values $B_p(t)$ by $P(A|B_p(t))$. Using these notations, we are now ready to formulate the definition of causality [7].

Given time series $X(t)$ and $Y(t)$, $Y(t)$ is defined to be causal to $X(t)$, if and only if:

$$\left\| X(t) - P(X(t)|U) \right\|^2 < \left\| X(t) - P(X_t|U - Y_p(t)) \right\|^2. \tag{2}$$

If our information set consists only of observations from two sequences $X(t)$ and $Y(t)$, the set $U(t)$ defined above would be:

$$U(t) = \{(X(t-k), Y(t-k))|k = 1,2,\dots\},$$

$$U(t) - Y_p(t) = \{X(t-k)|k = 1,2,\dots\}.$$

If we define the optimum unbiased least-square predictor to be a linear predictor, we then have:

$$P\left(X(t)\big|Y_p(t)\right) = \sum b_k Y(t-k) \,;\, k = 1,2,\dots \tag{3}$$

And $Y(t)$ is Granger causal to $X(t)$ if and only if:

$$\left\|X(t) - \sum a_m X(t-m) - \sum b_k Y(t-k)\right\|^2 < \|X(t) - \sum a_m X(t-m)\|^2, k, m = 1,2,\dots \tag{4}$$

In general, the predictor function can be non-linear. Only under the assumption that all the time series in the universe are Gaussian, the optimal predictor will have a linear form. However, a linear predictor can still be used to assess causality [7]. This linear predictor can be written as the following multivariate autoregressive equation:

$$X(t) = \sum a_m X(t-m) + \sum b_k Y(t-k) + e_x(t) \,;\, k, m > 0. \tag{5}$$

where $e_x(t)$ is the component of $X(t)$ that is uncorrelated with both the past of $X(t)$ and $Y(t)$. Based on the definition given above, $Y(t)$ is causal to $X(t)$ if and only if the optimal predictor uses $Y(t-k)$ to predict $X(t)$; at least one of the coefficients b_k is non-zero. Given finite recordings from the times series, one can use well known least-squares methods to estimate the coefficients of the model [11]–[13].

The above definition of causality can be easily extended to multivariate case:

$$X_1(t) = \sum a_{11}(k)X_1(t-k) + \ldots + \sum a_{N1}(k)X_N(t-k) + e_1(t),$$

$$X_2(t) = \sum a_{12}(k)X_1(t-k) + \ldots + \sum a_{N2}(k)X_N(t-k) + e_2(t),$$

$$\ldots$$

$$X_N(t) = \sum a_{1N}(k)X_1(t-k) + \ldots + \sum a_{NN}(k)X_N(t-k) + e_N(t).$$

A time series, $X_i(t)$, is then causal to another, $X_j(t)$, if and only if at least one of the coefficients $a_{ij}(k)$ is non-zero [13]. Based on these equations, it is possible to evaluate the strength of causal relationships among multiple random variables in the frequency domain by simply taking the Fourier transform of the estimated multivariate autoregressive equations.

1.2. Multi Variate Auto Regressive (MVAR) Coefficient Estimation

An iterative method for estimating the parameters of an autoregressive equation for the simple univariate case is described below; generalization of this method to a multivariate case is a straight forward task [11]–[13].

Consider the problem of predicting the future of a time series based on its P past values; that is we wish to predict $X(t)$ based on $X(t-k), k = 1,2, \ldots$. Assume that we are using a linear predictor:

$$\hat{X}(t) = \sum a_m X(t - m) \quad m = 1,2,3..P. \qquad (6)$$

Our task is to select the coefficients $a_m, m = 1,2,..,P$, such that the prediction $\hat{X}(t)$ is as close as possible to the actual value of $X(t)$. Hence, we have the following optimization problem:

$$\min_{a_m, m=1,..,P} |X(t) - \hat{X}(t)|^2 = \min_{a_m, m=1,..,P} |e_x(t)|^2. \qquad (7)$$

The solution to this equation is known as the forward prediction filter. By taking the derivative of the variance of the error, $|e_x(t)|^2$, with respect to every coefficient, a_m, we get the following set of equations:

$$< X_t X_{t-1} > = \sum a_m < X_{t-1} X_{t-m} >,$$

.

.

$$< X_t X_{t-k} > = \sum a_m < X_{t-k} X_{t-m} >,$$

.

.

$$< X_t X_{t-P} > = \sum a_m < X_{t-P} X_{t-m} >,$$

$$m = 1,2,...,P.$$

Where $< X_t X_{t-k} >$ represents the inner product of X_t and X_{t-k}. We can represent these equations in matrix form as below [13]:

$$R_k = < X_t X_{t-k} > .$$

$$
\begin{array}{l}
R_1 \\ \vdots \\ R_k \\ \vdots \\ R_P
\end{array}
=
\begin{array}{llll}
R_0 & R_1 & R_{P-1} \\ \vdots & \vdots \\ R_{k-1} & R_{k-2} & R_{k-P} \\ \vdots & \vdots \\ R_{P-1} & R_{P-2} & R_0
\end{array}
*
\begin{array}{l}
a_1 \\ \vdots \\ a_P
\end{array} .
$$

Using the Gaussian elimination method, we can change the matrix to an upper triangular matrix and solve for the coefficients using back substitution. However, it is interesting to see what elimination steps imply. In the first elimination step, all the elements of the first column, except R_0 are changed to zero. Let us represent the above matrix equation as:

$$
\begin{array}{l}
X_{t-1} \\ \vdots \\ X_{t-k} \\ \vdots \\ X_{t-P}
\end{array}
* X_t =
\begin{array}{l}
X_{t-1} \\ \vdots \\ X_{t-k} \\ \vdots \\ X_{t-P}
\end{array}
* [X_{t-1} \, . \, X_{t-k} \, . \, X_{t-P}] *
\begin{array}{l}
a_1 \\ \vdots \\ a_P
\end{array} .
$$

Each element of the (Px1) vector on the left-hand side of the equation represent the inner product of X_{t-k} with X_t. Hence the right-hand side of this equation represents the same matrix as the previous equation. I will use the same notation for the inner product in the rest of this chapter. The first elimination step can then be re-written as:

$$\begin{bmatrix} X_{t-1} \\ . \\ e^1_{t-k} \\ . \\ e^1_{t-P} \end{bmatrix} * X_t = \begin{bmatrix} X_{t-1} \\ . \\ e^1_{t-k} \\ . \\ e^1_{t-P} \end{bmatrix} * [X_{t-1} \;.\; X_{t-k} \;.\; X_{t-P}] * \begin{bmatrix} a_1 \\ \vdots \\ a_P \end{bmatrix}.$$

Where

$$e^1_{t-k} = X_{t-k} - \frac{< X_{t-k} * X_{t-1} >}{|X_{t-1}|^2} X_{t-1}.$$

(8)

e^1_{t-k} represents the component of X_{t-k} that is uncorrelated with X_{t-1}. If we continue the elimination until the last step, we then would have:

$$\begin{bmatrix} X_{t-1} \\ e^1_{t-2} \\ . \\ . \\ e^{1,2,3..,(k-1)}_{t-k} \\ . \\ . \\ e^{1,2,3,..,P-2}_{t-P+1} \\ e^{1,2,3,..,P-1}_{t-P} \end{bmatrix} * X_t = \begin{bmatrix} X_{t-1} \\ e^1_{t-2} \\ . \\ . \\ e^{1,2,3..,(k-1)}_{t-k} \\ . \\ . \\ e^{1,2,3,..,P-2}_{t-P+1} \\ e^{1,2,3,..,P-1}_{t-P} \end{bmatrix} * [X_{t-1} \;..X_{t-k} \;... \; X_{t-P}] * \begin{bmatrix} a_1 \\ \vdots \\ a_P \end{bmatrix}.$$

Where $e_{t-k}^{1,2,3..,(k-1)}$ represents the component of X_{t-k} that is uncorrelated with $X_{t-1}, X_{t-2}, ..., X_{t-k+1}$. Now assume that we have solved for the coefficients $a_1, .., a_p$ and define the residual as:

$$E_t^P = X_t - \sum a_m X(t-m) \quad m = 1,2,3..P.$$

(9)

We now wish to increase our model order and solve for the coefficient a_{P+1}. We then have to solve for the following equation:

$$
\begin{bmatrix} X_{t-1} \\ e_{t-2}^1 \\ . \\ . \\ e_{t-k}^{1,2,3..,(k-1)} \\ . \\ . \\ e_{t-P}^{1,2,3,..,P-1} \\ e_{t-P-1}^{1,2,3,..,P} \end{bmatrix} * X_t = \begin{bmatrix} X_{t-1} \\ e_{t-2}^1 \\ . \\ . \\ e_{t-k}^{1,2,3..,(k-1)} \\ . \\ . \\ e_{t-P}^{1,2,3,..,P-1} \\ e_{t-P-1}^{1,2,3,..,P} \end{bmatrix} * [X_{t-1} \, .. X_{t-k} ... \, X_{t-P} \, X_{t-P-1}] * \begin{bmatrix} a^{P+1}_1 \\ \vdots \\ a_P^{P+1} \\ a_{P+1} \end{bmatrix}.
$$

We can use our solution for the model order of P to solve for the model order of P+1. In the first step, we can easily solve for a_{P+1} as the above matrix is upper triangular:

$$a_{P+1} = \frac{< X_t, e_{t-P-1}^{1,2,3,..,P} >}{\left| e_{t-P-1}^{1,2,3,..,P} \right|^2} = \frac{< E_t^P, e_{t-P-1}^{1,2,3,..,P} >}{\left| e_{t-P-1}^{1,2,3,..,P} \right|^2}.$$

(10)

We then back-substitute the value for a_{P+1} in our equations:

$$
\begin{bmatrix} X_{t-1} \\ e^1_{t-2} \\ \cdot \\ \cdot \\ \cdot \\ e^{1,2,3..,(k-1)}_{t-k} \\ \cdot \\ \cdot \\ \cdot \\ e^{1,2,3,..,P-1}_{t-P} \end{bmatrix} * \left(X_t - a_{P+1}X_{(t-P-1)}\right) = \begin{bmatrix} X_{t-1} \\ e^1_{t-2} \\ \cdot \\ \cdot \\ \cdot \\ e^{1,2,3..,(k-1)}_{t-k} \\ \cdot \\ \cdot \\ \cdot \\ e^{1,2,3,..,P-1}_{t-P} \end{bmatrix} * \ [X_{t-1} \ ..X_{t-k} \ ... \ X_{t-P} \ ] * \begin{bmatrix} a^{P+1}_1 \\ \vdots \\ a^{P+1}_P \end{bmatrix} .
$$

Note that the solution for the new values of the coefficients $a^{P+1}_1,..,a^{P+1}_p$ can now be written as:

$$
\begin{bmatrix} a^{P+1}_1 \\ \vdots \\ a^{P+1}_P \end{bmatrix} = \begin{bmatrix} a_1 \\ \vdots \\ a_P \end{bmatrix} - a_{P+1} \begin{bmatrix} \Delta_P \\ \vdots \\ \Delta_1 \end{bmatrix} .
$$

Where Δ_i's are the solution to the following matrix equation:

$$
\begin{bmatrix} X_{t-1} \\ e^1_{t-2} \\ \cdot \\ \cdot \\ \cdot \\ e^{1,2,3..,(k-1)}_{t-k} \\ \cdot \\ \cdot \\ \cdot \\ e^{1,2,3,..,P-1}_{t-P} \end{bmatrix} * \left(X_{(t-P-1)}\right) = \begin{bmatrix} X_{t-1} \\ e^1_{t-2} \\ \cdot \\ \cdot \\ \cdot \\ e^{1,2,3..,(k-1)}_{t-k} \\ \cdot \\ \cdot \\ \cdot \\ e^{1,2,3,..,P-1}_{t-P} \end{bmatrix} * \ [X_{t-1} \ ..X_{t-k} \ ... \ X_{t-P} \ ] * \begin{bmatrix} \Delta_P \\ \vdots \\ \Delta_1 \end{bmatrix} .
$$

This equation is known as the backward prediction filter as it is the solution to the following equations [11], [13]:

$$\check{X}(t) = \sum \Delta_m X(t + m), \, m = 1,2,..,P. \tag{11}$$

$$\check{X} \min_{\Delta_m, m=1,2,...,P} |X(t) - \check{X}(t)|^2. \tag{12}$$

Hence the iterative solution to the AR coefficients consists of solving for the parameters in both the forward prediction filter and the backward prediction filter, a_m and $\Delta_m, m = 1,2,..,P$. We then have to calculate the residual for both the forward prediction and the backward prediction filters. Using the backward and the forward residual, defined similarly as in equation 9, we solve for the new coefficients a_{P+1}, Δ_{P+1}. After back-substituting the values of the new coefficients a_{P+1}, Δ_{P+1} , we can update the coefficients a_m and $\Delta_m, m = 1,2,..,P$ through the following equations:

$$\begin{matrix} a_1^{P+1} \\ \vdots \\ a_P^{P+1} \end{matrix} = \begin{matrix} a_1 \\ \vdots \\ a_P \end{matrix} - a_{P+1} \begin{matrix} \Delta_P \\ \vdots \\ \Delta_1 \end{matrix}.$$

$$\begin{pmatrix} \Delta_1^{P+1} \\ \vdots \\ \Delta_P^{P+1} \end{pmatrix} = \begin{pmatrix} \Delta_1 \\ \vdots \\ \Delta_P \end{pmatrix} - \Delta_{P+1} \begin{pmatrix} a_P \\ \vdots \\ a_1 \end{pmatrix}.$$

Chapter 2

EEG Source and Sink Maps at Resting State With Eyes Open

As was described in Chapter 1, it is possible to evaluate the strength of causal relationships among multiple random variables in the frequency domain by taking the Fourier transform of the estimated multivariate autoregressive equations. In this section, I will show how to employ this technique to define a measure that describes the degree wherein each channel can be considered a source of information or a sink.

2.1. Introduction

Direct Transfer Function as proposed in [14] provides a measure of connectivity and information transfer among two channels in a multivariate setting. Consider a single channel, channel j, having connections of varying strengths to M separate channels. Among the channels in this collection, consider a particular channel, channel i. In this setting, the information going from channel i to channel j comprises of only a certain portion of all the information that is being transmitted to the sink channel. If the strength of connection from channel i to channel j is significantly higher compared to other channels, then almost all the information going to channel j is coming from this single source. That is, altering this source would significantly affect the behavior of the sink channel. On the other hand, if this connection is weak, then only a minor portion of the information transmitted to this channel is from that particular source and removing this source from the environment would not affect the behavior of the sink channel. DTF from a source channel to a sink channel is a quantitative measure of the ratio of the

information transferred to the sink from the source to the total information influx from all other channels in the environment.

2.1.1. Source Maps

The mathematical formulation of DTF based on the intuitive description provided above is simple. After estimating the coefficients for the multivariate autoregressive equation, using the Fourier transform, I represent the same set of equations in the frequency domain:

$$X(t) = [X_1(t)\, X_2(t) \dots X_M(t)]',$$

$$X(t) = \sum_{k=1}^{P} A(k)X(t-K) + e(t),$$

$$X(f) = A(f)X(f) + e(f),$$

$$X(f) = \big(I(f) - A(f)\big)^{-1} e(f),$$

$$X(f) = H(f)e(f),$$

$$x_j(f) = \sum_{i=1}^{N} h_{ji}(f)e_i(f).$$

The $h_{ji}(f)$ coefficients in the above equation represent the strength of connection from channel i to channel j; $h_{ji}(f)$ corresponds to the element in the j_{th} row and i_{th} column of the matrix H. DTF can then be calculated using the following normalization scheme:

$$DTF_{ji} = \frac{|h_{ji}|^2}{\sum_{i=1}^{N}|h_{ji}|^2}. \tag{13}$$

DTF is a normalized measure and represents the ratio of the variance coming from the source channel to the sink channel to the total influx of variance from every other channel in the environment. One can then think of DTF as a normalized measure that describes how much a particular channel can be considered a source for another channel in the environment. Averaged across every channel in the environment, DTF then provides a normalized measure of how much a particular channel can be considered a source in the environment under investigation:

$$Source_i = \frac{\sum_{j=1, j \neq i}^{N} DTF_{ji}}{N}. \tag{14}$$

2.1.2. Sink Maps

By using the Source coefficients to represent the flow of information in the environment, we lose information on the directionality of connections. Furthermore, DTF is a measure that emphasizes sources. Consider two independent channels that are not causal to the other channels in the environment. Assume that one of the channels is receiving significant information from all other channels while the second channel is completely separate and independent from the environment and the sources within it. These two

15

channels would have identical Source coefficients, equal to zero, and in a map that shows the source activity of all the channels, these two would be indistinguishable.

Following the same line of reasoning that lead to the definition of DTF, we can define a new measure to assess how much information a channel is receiving from its surrounding environment. Consider the equation below:

$$X(f) = H(f)e(f). \tag{15}$$

Each column in the transfer matrix, H, represents the total outflow from a particular source. Elements of this column then account for the portion of the total outflow that is being transmitted to different channels in the medium. Hence the following normalized measure can be used to describe the part of the outflow of channel i that channel j is receiving:

$$\lambda_{ji} = \frac{|h_{ji}|^2}{\sum_{j=1}^{N}|h_{ji}|^2}. \tag{16}$$

$h_{ji}(f)$ corresponds to the element in the j$_{th}$ row and the i$_{th}$ column of H. λ_{ji} then shows the percentage of information that is being transferred to channel j to the total outflow from channel i. Averaged across every channel, the above coefficient then provides a normalized measure of how much a particular channel can be considered a sink in the environment under investigation:

$$Sink_j = \frac{\sum_{i=1,i\neq j}^{N} \lambda_{ji}}{N}.$$

<div align="right">(17)</div>

It is important to note that the relation among pairs of channels is not necessarily of the form of a uni-directed connection, that is a source to sink relation. Feedback can exist among a pair of channels, and the channels can behave both as a source and a sink in relation to each other. If feedback is identified among two channels, it is possible to find one channel of the pair to be the source at a particular frequency band while at another frequency band the same channel can be identified to be the sink.

2.2. Methods

2.2.1. Subject and Setting

EEG data was collected by Mr. Olajide Babewale and Ms. Tien Nguyen from the Bioengineering Department of the University of Texas at Arlington. EEG data was collected from 8 subjects at resting states with the eyes open using an EEG- fNIRs multimodal head cap with 64 EEG electrodes and 133 fNIRs channels. EEG electrode locations in this cap are not in exact alignment with the standard 10-10 EEG international system. However, for convenience, and as the electrode locations were close to their original position in the 10-10 system, in the rest of this thesis I approximated the actual EEG electrode locations with those of the standard 10-10 system. The EEG data was collected using the Biosemi EEG machine. The sampling rate of the EEG collection system was set to 1024 Hz. During the recording of the data, subjects were instructed to sit still in a chair. EEG was then recorded for each subject for five minutes.

2.2.2. EEG Signal Preprocessing

Data was imported to MATLAB using EEGLAB toolbox [15]. Following preprocessing steps were taken:

1. Cz was chosen as the reference electrode when importing the data to MATLAB.

2. The baseline of each channel was removed.

3. From 64 electrode readings, only the following thirty channels were retained for further analysis: **Fpz Fp1 Fp2 F7 F3 Fz F4 F8 FC5 FC1 FC2 FC6 T7 C1 C3 C2 C4 T8 CP5 CP1 CP2 CP6 P7 P3 Pz P4 P8 O1 O2 Oz,** see figure 1. I opted to use fewer electrodes to increase numerical precision when estimating the parameters for the multivariate autoregressive equations (MVAR).

4. Recordings were visually examined to identify corrupted channels. The corrupted electrodes were then removed from the data set.

5. For each subject, the first epoch of distortion with high electrical noise was visually identified. EEG recordings only up to that point of time were extracted and used for analysis.

6. High-frequency noise and low-frequency trends were removed from the data using a zero-phase bandpass filter with cut-off frequencies at 0.4 and 40 Hz.

7. Data was down-sampled to 256 Hz.

8. Using the independent component analysis (ICA) module of the EEGLAB, ocular artifacts were identified and removed.

2.2.2.1 EEG Channel Location

The following figure shows the location of the selected EEG channels. I have used the standard BESA coordinates, extracted from the EEGLAB, to show the EEG electrode locations. In this coordinate system, the x-axis passes through the left and right pre-auricular, LPA and RPA; positive values for x correspond to the right hemisphere. The y-axis is orthogonal to the x-axis and passes through the nasion; electrodes with positive y-values are on the anterior side. The scale of the x and the y-axis are chosen such that human head radius on this scale is 80.
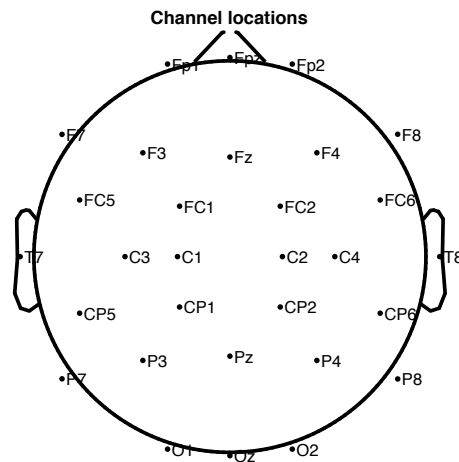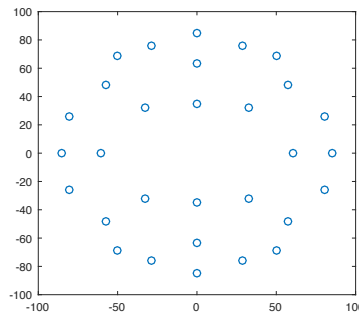
Figure 1. Location of the selected EEG electrodes.

2.2.3. Model Order and Window Size Selection

I divided the EEG recording to overlapping windows of equal length. I then estimated the set of MVAR parameters that best described the data in each window. The size of the window should be large enough so as to allow for a statistically reliable estimation of the MVAR parameters and short enough so as to not void the assumption of stationarity. The model order for EEG connectivity in the literature varies between 3 and 10. Akaike suggests that for a given particular recording, the number of estimated coefficients should not be higher than P_m[17]:

$$P_m = 3 * (N)^{\frac{1}{2}}. \tag{18}$$

Where N is the number of available data points. Since for a multichannel recording the number of estimated coefficients in an MVAR of order P is $M^2 P$, M being the number of channels, I can find the following lower bound limit on the number of data points required for estimating an MVAR model of order P:

$$N > \frac{(MP)^2}{3}. \tag{19}$$

For a recording with 29 channels, to be able to reliably estimate the coefficients for a 10th degree MVAR model, I then need to at least have 36.5 seconds of recording. Optimal model order for window size of 35 seconds was estimated using Akaike Information Criteria:

$$AIC(P) = N * \ln\left(det\left(U_p\right)\right) + 2M^2P. \qquad\qquad (20)$$

Where N is the length of the recordings, is the covariance matrix of the residual noise, P is the chosen model order, and M is the number of channels. This index was calculated for models of increasing order, from one to ten; the optimal model is the one that has the lowest index. Using this criterion, the optimal model order was calculated for multiple windows. It was found that optimal model order for most of the windows was either 6 or 7.

Data was then divided into overlapping windows of length of 35 seconds; each window overlapped the previous window for 32 seconds, see figure 2. I then calculated the set of MVAR parameters that best described the data in each window. Before estimating these MVAR coefficients, the data was normalized by dividing it by its corresponding variance [16].
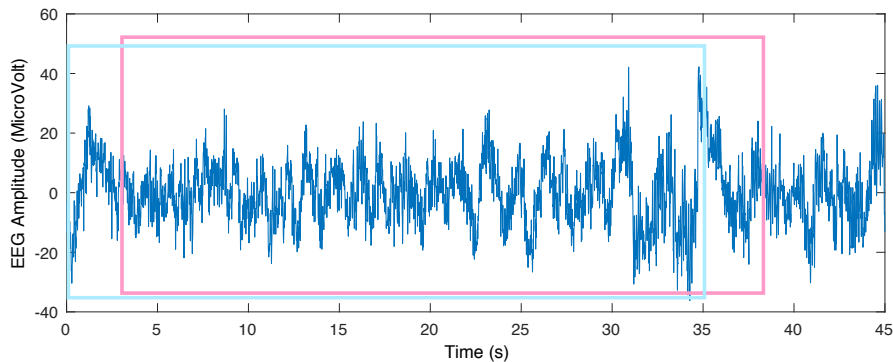
Figure 2. Division of EEG data into overlapping windows of length of 35 seconds. Each window overlapped the previous window for 32 seconds. The figure shows two example windows.

2.2.4. Estimation of MVAR parameters

MVAR parameters were estimated using two different methods. In the first method, MVAR parameters were estimated using the iterative Yule-Walker formulation described earlier in the first chapter [12]; this algorithm was implemented in MATLAB. As was mentioned in section 2.3.3, the optimal model order varied between six and seven across different windows. Hence I decided to use two model orders, six and seven, for estimating MVAR coefficients when using this algorithm.

In the second method, MVAR parameters were estimated using the eConnectome toolbox in MATLAB [18]. This algorithm uses a direct QR factorization with a regularization factor to estimate the MVAR coefficients. The model order chosen by this algorithm is based on Schwarz's Bayesian Criterion[18]; the optimal model order chosen by this toolbox was 10.

2.2.5. Source and Sink Coefficients

After estimating the MVAR parameters using the above two methods, direct transfer function (DTF) coefficients were calculated by taking the Fourier transform of the resulting equations; note that to achieve a frequency resolution of 1Hz, the impulse responses were zero padded accordingly. From the DTF coefficients, source and sink maps were calculated using the methods described in section 2.1.1 and 2.1. 2. Source and sink coefficients for the alpha band, 8-12 Hz, and the theta band, 4-8 Hz, were calculated by averaging the values within the respective bands. While it is possible to compute the

source and the sink coefficients for also the gamma and the beta band, I preferred to focus my analysis on only the alpha and the theta band. I opted to examine the changes in connectivity only in these two bands before possibly extending the same method to all the frequency bands.

2.2.6. Spectral Power Density

Furthermore, I also calculated the power spectrum using the Welch method [19]. EEG recordings were divided into non-overlapping windows of 9 seconds. Welch power spectrum in each window was calculated using the following specifications for the Welch algorithm:

- Number of windows: Eight.

- Length of the windows: Two seconds.

- Percentage of overlap: 50%; each window overlapped the previous window for one seconds.

- Final frequency resolution: 0.5 Hz.

2.3. Results

2.3.1. Spectral Power Density in the Alpha and the Theta Band

Estimated power spectrum was averaged across all subjects and all windows. Afterward, the average power in the alpha band (8-12 Hz) and the theta band (4-8 Hz) was computed. The results are plotted in Figure 3.

As it can be seen from Figure 3, the electrodes in the frontal region have a higher power in the theta band while the electrodes at posterior location show higher power in the alpha
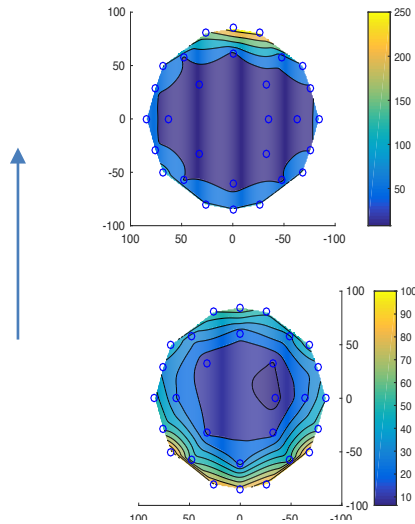
Figure 3. The upper plot shows the spatial distribution of power in the theta band. The lower plot shows the spatial distribution of the power in the alpha band. The x-axis and the y-axis show the Cartesian BESA coordinate for the electrodes. Circles mark the location of the electrodes. The arrow points toward the anterior part of the head. The colorbar shows the energy ($MicroVolt^2$).

band. The power, whether in the alpha or in the theta band, is localized to frontal and occipital regions.

2.3.2. Source Maps

The resulting source and sink coefficients in the alpha band and the theta band were averaged across eight subjects and all windows. Figures 4 and 5 show the source maps for the theta and the alpha band. Both figure 4 and figure 5 consist of three plots. The leftmost plot in each figure shows the resulting source map when the iterative Yule-Walker equation of order six was used to estimate the MVAR coefficients. The middle plots in the figures 4 and 5 show the source map when the iterative Yule-Walker equation of order seven was used to estimate the MVAR coefficients. The rightmost plots show

the source map when eConnectome toolbox in MATLAB was used to assess the MVAR parameters. Comparing these three plots in the figures 2 and 3, we see that these different methods give strikingly similar results.

For the theta band, irrespective of the algorithm, one can see that sources are located in the frontal and occipital regions (see Figure 4). However, sources in the frontal region have much higher source coefficients compared to those in the occipital region. Sources in the frontal region were identified to provide 16 percent of the total transmitted information while sources in the occipital region only accounted for 2 percent of the total information flux.

For the alpha band, the same distribution of sources can be observed, see figure 5. Sources are localized to the frontal and occipital regions, with sources in the frontal region having much higher source coefficients.

.

Figure 4. Source map at Theta Frequency band. The leftmost plot shows the resulting source map when MVAR parameters were estimated using iterative Yule-Walker estimation method with a model order of six. The middle plot shows the same map when using a model order of seven. The rightmost plot shows the resulting source map using MVAR coefficients estimated with the eConnectome toolbox. The x-axis and the y-axis show the Cartesian BESA coordinate for the electrodes. Circles mark the location of the electrodes. The arrow points toward the anterior part of the head. The colorbar shows the source coefficient. How to read the map: in the leftmost plot, for example, the dark blue colored region around Cz has a source coefficient of about 0.02. A source coefficient of 0.02 means that these locations account for about 2% of the total information transmitted in the medium. On the other hand, in the same plot, the frontal regions have a source coefficient of 0.14. That is frontal regions account for the 14% of the total information transmitted in the medium.
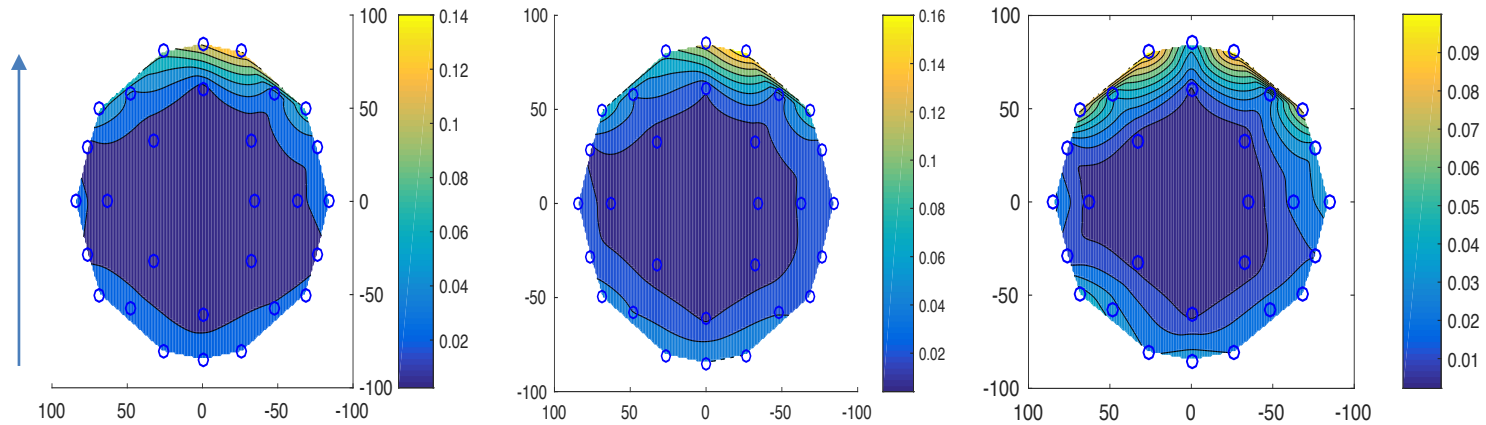
Figure 5. Source map at Alpha Frequency band. The leftmost plot shows the resulting source map when MVAR parameters were estimated using iterative Yule-Walker estimation method with a model order of six. The middle plot shows the same map when using a model order of 7. The rightmost plot shows the resulting source map using MVAR coefficients estimated with the eConnectome toolbox. The x-axis and the y-axis show the Cartesian BESA coordinate for the electrodes. Circles mark the location of the electrodes. The arrow points toward the anterior part of the head. The colorbar shows the source coefficient. How to read the map: in the leftmost plot, for example, the dark blue colored region around Cz has a source coefficient of about 0.02. A source coefficient of 0.02 means that these locations account for about 2% of the total information transmitted in the medium. On the other hand, in the same plot, the frontal regions have a source coefficient of 0.14. That is frontal regions account for the 14% of the total information transmitted in the medium.
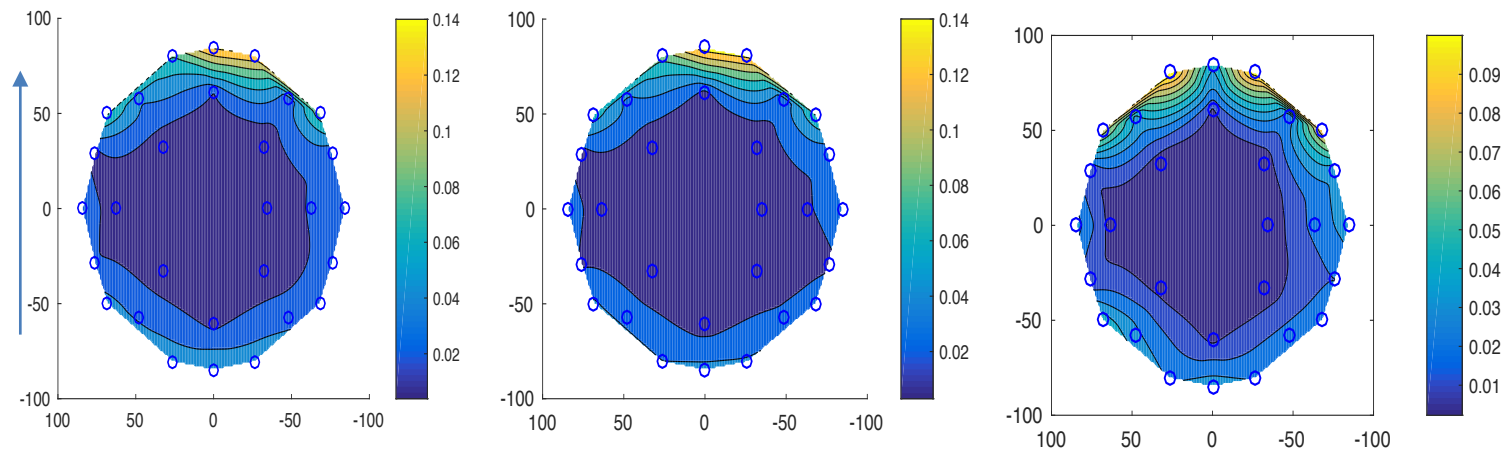
2.3.3 Sink Maps

Figures 6 and 7 show the sink maps for the theta and the alpha band. These figures have similar features to those of Figure 4 and 5. Both figure 6 and figure 7 consist of three plots. The leftmost plot in each figure shows the resulting sink map when the iterative Yule-Walker equation of order six was used to estimate the MVAR coefficients. The middle plots in the figures 6 and 7 show the sink map when the iterative Yule-Walker equation of order seven was used to assess the MVAR coefficients. The rightmost plots show the sink map when eConnectome toolbox in MATLAB was used to estimate the MVAR parameters. Comparing these three plots in the figures 6 and 7, we see that these different methods give strikingly similar results.

Sinks in the theta band have a distribution opposite to the sources; see figure 6. Very few sinks are observable at the frontal and the occipital regions. Most of the sinks are localized to the area bounded by the electrodes C3-C4-FC1-FC2-CP1-CP2. Electrode C3 was identified to have the highest sink coefficient, receiving about 10% of the total information that is transmitted in the environment.

From figure 7 we can observe that the sinks in the alpha band are also localized to the region bounded by electrodes C3-C4-FC1-FC2-CP1-CP2. Electrode C3 was again identified to be the major sink of the environment. About 10% of the total information flow is being transmitted to this site.

28

Figure 6. Sink map at Theta Frequency band. The leftmost plot shows the resulting source map when MVAR parameters were estimated using iterative Yule-Walker estimation method with a model order of 6. The middle plot shows the same map when using a model order of 7. The rightmost plot shows the resulting source map using MVAR coefficients estimated with the eConnectome toolbox. The x-axis and the y-axis show the Cartesian BESA coordinate for the electrodes. Circles mark the location of the electrodes. The arrow points toward the anterior part of the head. The colorbar shows the sink coefficient. How to read the map: in the leftmost plot, for example, the dark blue colored region around Fpz has a sink coefficient of about 0.02. A sink coefficient of 0.02 means that these locations receive about 2% of the total information transmitted in the medium. On the other hand, in the same plot, the central regions have a source coefficient of 0.10. That is the regions around C3 receive 10% of the total information transmitted in the medium.
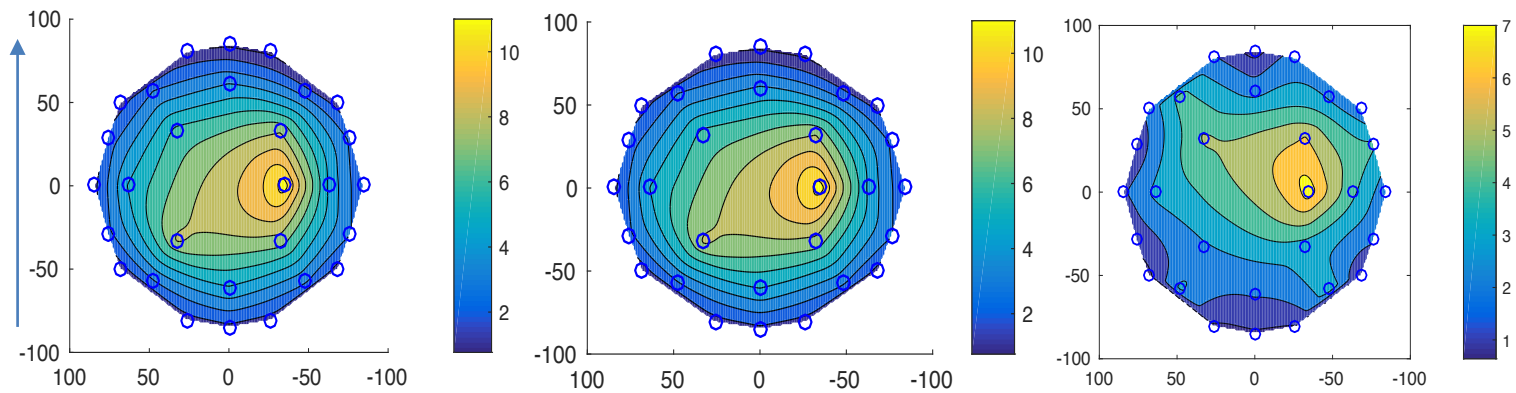
Figure 7. Sink map at Alpha Frequency band. The leftmost plot shows the resulting source map when MVAR parameters were estimated using iterative Yule-Walker estimation method with a model order of 6. The middle plot shows the same map when using a model order of 7. The rightmost plot shows the resulting source map using MVAR coefficients estimated with the eConnectome toolbox. The x-axis and the y-axis show the Cartesian BESA coordinate for the electrodes. Circles mark the location of the electrodes. The arrow points toward the anterior part of the head. The colorbar shows the sink coefficient. How to read the map: in the leftmost plot, for example, the dark blue colored region around Fpz has a sink coefficient of about 0.02. A sink coefficient of 0.02 means that these locations receive about 2% of the total information transmitted in the medium. On the other hand, in the same plot, the central regions have a source coefficient of 0.10. That is the regions around C3 receive 10% of the total information transmitted in the medium.
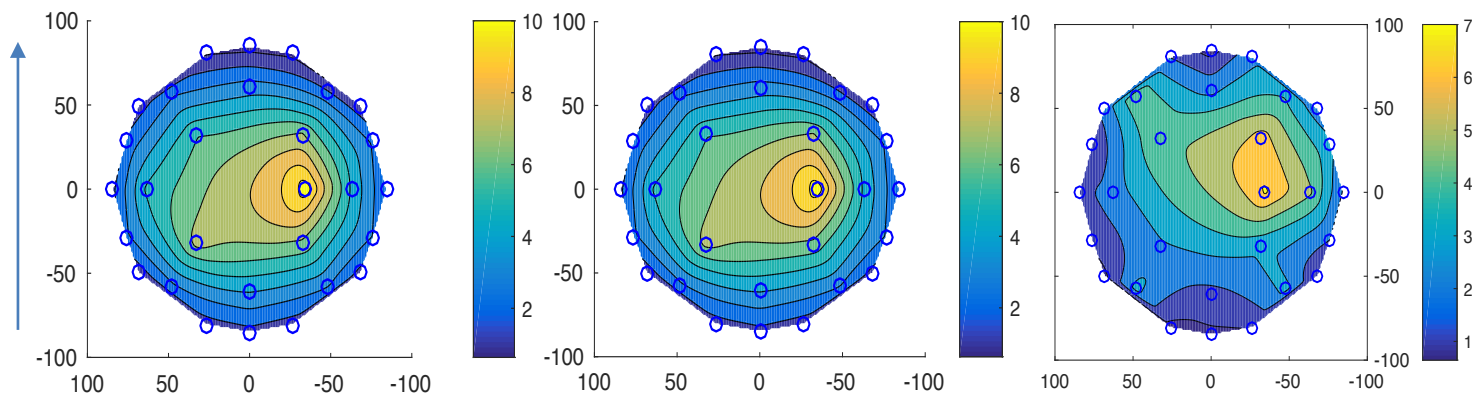
2.4. Disscussions

It is known that in the resting state with the eyes open condition, the power spectral density in the alpha band is dominant in posterior areas while frontal regions have a significantly higher power in theta band [20, 21]. My results are consistent with these previous findings. The following figure compares my results with those reported in [20]; both topographical maps show significant theta activity in the frontal regions and significant alpha activity in the occipital regions; compare the third column of the left plot at theta and alpha band with the right plot.
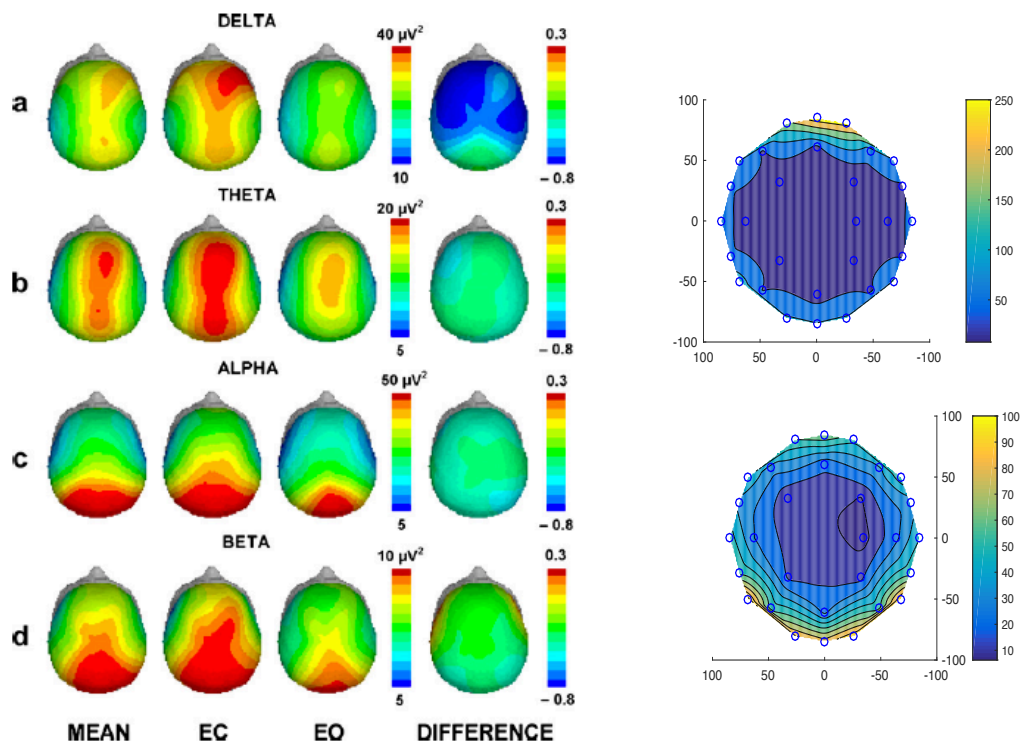
Figure 8. In the resting state with the eyes open condition, the third column of the left plot, significant theta activity in the frontal regions and significant alpha activity in the occipital regions can be observed. The left plot is taken from [20]. My findings, the right plot shows similar results. At theta frequency band, upper figure of the left plot, a significant activity can be observed in the frontal regions. At alpha band, significant activity can be observed in the occipital regions.

31

Few studies have examined the information flow in the human brain in the resting state with the eyes open. In [21] causal information flow in the eyes open resting condition was studied using EEG recordings from 64 channels. They report that in both the theta (3Hz) and the alpha (10Hz) band, the anterior cingulate is the dominant source of information which sends information to dorsolateral prefrontal cortices. My results show similar localization of sources and sinks; I found that in both Theta and Alpha band, source activity is localized to frontal electrodes, Fpz, Fp1, Fp2, and that the sinks of information are predominantly localized to the region bounded by the electrodes C3-C4-FC1-FC2-CP1-CP2. In [22], using EMG recordings, the sources of information in the theta band were identified to be dominantly at the frontal cortex. However, unlike my findings and those reported in [21], they report that in the alpha band the sources of information are localized at the occipital region.

This discrepancy in the direction of information flow can also be seen in the studies of connectivity in the resting condition with the eyes closed. In [9], sources of information at alpha band were reported to be dominantly the posterior electrodes O2, Oz and P4; it is interesting to note that similar to my finding, they also did not observe any propagation from the temporal electrodes. Similar results regarding source localization in the resting condition with the eyes open have been reported in [23], [22], and [21]. On the other hand, in [24], [25] and [26] significant information flow from anterior to posterior regions of the brain have been reported. Hillebrand et al. suggests that these discrepancies

32

in the direction of information flow are due to the effects of referencing EEG, and hence argues that MEG would be a more suitable modality to study information flow [22]. However, it is to note that both [23] and [25] have referenced their EEG to linked mastoid, and their results still show opposite directions for information flow in the alpha band.

Chapter 3

Is EEG Causal to fNIRs?

3.1. Introduction

Functional near infrared spectroscopy (fNIRs) and functional magnetic resonance imaging (fMRI) measure the hemodynamic fluctuations in the brain. They can be used to assess brain activity through studying the local changes in oxyhemoglobin concertation and blood flow. Understanding the relation between hemodynamic fluctuations and the underlying neural activity is crucial in interpreting the signals acquired in fNIRs and fMRI. Through the simultaneous recording of both the neural activity and the hemodynamic changes, one can identify the correlates of various neuronal events in the local changes of blood flow. Investigations of the neural-hemodynamic coupling can be found in numerous papers[27]–[31].

Using tools from the linear time invariant system analysis, Logothetis et. al. shows that the changes in the blood flow measured through fMRI can be represented as a linear function of the simultaneously recorded local field potentials [30], [31]. By calculating the cross-covariance function of the neural activity and the BOLD response, he estimates the hemodynamic response function (HRF) that relates these two modalities. The waveform corresponding to the convolution of the HRF with the recorded neural activity can then serve as a predictor of the hemodynamic response.

It has now become a usual practice to investigate the neural underpinnings of hemodynamic events by convolving the recorded neural activity with the standard HRF [32] and calculating the correlation of the resulting waveform with the measured hemodynamic response [33]–[35]. It is important to note that this correlation analysis, however, does not indicate causality. A more suitable mathematical formulation that can be used to assess causality across these two modalities is the Granger causality measure [7][10].

An important research area where the cross-covariance analysis is currently being used is the identification of the generators of the alpha rhythm in the brain [33]– [35]. Alpha rhythm is the oscillations of the electrical activity of the brain within 8-12 Hz. The neural generators of this rhythm have not been yet identified [36]. It is possible to determine the areas wherein the hemodynamic fluctuations are correlated with the alpha rhythm changes by the simultaneous measurement of both the EEG and the fMRI; these areas can then serve as a guide to identify the generators of alpha activity.

In the present experiment, I investigated the relation between simultaneously acquired EEG and fNIRs in the resting state with the eyes open. I examined if the brain's electrical activity at a particular electrode site is causal to the recorded hemodynamic activity in the neighborhood of that EEG channel.

I then examined the hemodynamic fluctuations and their relation to the alpha rhythm changes that were measured in the occipital region. The cross-covariance analysis

identified a significant correlation between the alpha rhythm and the hemodynamic activity. Granger causality analysis, however, rejected the hypothesis that the recorded alpha rhythm is causal to the hemodynamic activity at any of the fNIRs recording sites.

3.2. Methods

3.2.1. Subject and Setting

Eight healthy volunteers participated in the study. They were instructed to sit still in a chair with their eyes open.

3.2.2. Registration of EEG and fNIRs

EEG and fNIRs signals were recorded simultaneously using the Biosemi EEG collection system and the Shimadzu fNIRs machine. Simultaneous measurement of these two signals was achieved by using a multimodal head cap with 64 EEG electrodes and 133 fNIRs channels. EEG electrode locations in this cap are not in exact alignment with the standard 10-10 EEG international system. However, for convenience, and as the electrode locations were close to their original position in the 10-10 system, in the rest of this thesis, I approximated the actual EEG electrode locations with those of the standard 10-10 system; for more details on EEG channel locations, please refer to the section 2.2.2.1. The sampling rate for the EEG collection system was set to 1024 Hz. fNIRs data was collected at 8 Hz. EEG data was imported to MATLAB using EEGLAB toolbox [2]. fNIRs data was imported to MATLAB using NIRS-SPM. The data was collected by Mr. Olajide Babewale and Ms. Tien Nguyen from the Bioengineering Department of the University of Texas at Arlington.

3.2.3. EEG and fNIRs Artifact Correction

EEG data preprocessing consisted of the following steps:

1. Cz was chosen as the reference electrode when importing the data to MATLAB.

2. The baseline of each channel was removed.

3. From the 64 electrode readings, only the following fifteen channels were retained for further analysis: **Fp1, F3, F7, C3, T7, O1, Pz, Fp2, Fz, F4, F8, C4, T8, O2, and Cz;** location of these electrodes are shown in figure 1. I opted to use fewer electrodes for this preliminary analysis and to test my hypothesis on a smaller set of data before possibly extending it to all the channels.

4. Recordings were visually examined to identify corrupted channels. The corrupted electrodes were then removed from the data set.

5. For each subject, the first epoch of distortion with high electrical noise was visually identified. EEG recordings only up to that point of time were extracted and used for analysis.

6. High-frequency noise and low-frequency trends were removed from the data using a zero-phase bandpass filter with cut-off frequencies at 0.4 and 40 Hz.

7. Data was down-sampled to 256 Hz.

8. Using the independent component analysis (ICA) module of EEGLAB, ocular artifacts were identified and removed.

fNIRs oxyhemoglobin data was recorded at sampling rate of 8 Hz. The fNIRs data was imported to MATLAB using NIRS-SPM toolbox. Preprocessing of fNIRs consisted of

bandpass filtering at cut-off frequencies of 0.1-0.4 Hz. Only the fNIRs channels located near the selected EEG channels were retained for further analysis, see table.1.

Table 1.EEG electrode and fNIRs channel pairs. The first and the third row show the selected EEG channels. The fNIRs channel selected corresponding to each EEG channel is written right below every EEG channel.

Fp1	F3	F7	C3	T7	O1	Pz	Fp2
5	20	26	60	58	12	113	7
Fz	F4	F8	Cz	C4	T8	O2	Fz
22	24	34	62	64	66	126	22

3.2.4. Causality Analysis

A times series, $Y(t)$ is Granger causal to another time series, $X(t)$, if and only if knowledge of the past of that time series, $Y(t-k), k = 1,2,3,..$, helps in predicting the present value of the other [7] [10].In general, the predictor function can be non-linear. Only under the assumption that all the time series in the universe are Gaussian, the optimal predictor will have a linear form. However, a linear predictor can still be used to assess causality [7]. This linear predictor can be written as the following multivariate autoregressive equation:

$$X(t) = \sum a_m X(t-m) + \sum b_k Y(t-k) + e_x(t) \, ; k, m > 0.$$

(21)

where $e_x(t)$ is the component of $X(t)$ that is uncorrelated with both the past of $X(t)$ and $Y(t)$. Based on the definition given above, $Y(t)$ is causal to $X(t)$ if and only if at least one of the coefficients b_k is non-zero. Given finite recordings from the times series, one can use well known least squares methods to estimate the coefficients of the model [11]- [13]. Wald statistics can then be used to assess if the null hypothesis that all the coefficients b_k are zero is either true or false.

Since EEG and fNIRs are collected at different sampling frequencies, the above formulation of causality should be modified as below

$$fNIRs(T) = \sum a_m fNIRs(T - m) + \sum b_{m,k} EEG(T - m, k) + e_{fNIRs}(T) \, ; k, m > 0. \tag{22}$$

Where T shows the time index in terms of the low-frequency series and the index k corresponds to k_{th} high-frequency sample of the EEG in each sampling period of the fNIRs. Hence $EEG(T - 1, 1)$ indexes the EEG sample collected right after the sample $fNIRs(T - 1)$ and $EEG(T - 1, M - 1)$ signifies the EEG sample collected just before $fNIRs(T)$; M is the sampling ratio between these two series.

Given that the EEG signal was sampled at 256 Hz and the fNIRs signal was collected at 8 Hz, a linear predictor of order one will have 33 unknown parameters:

$$fNIRs(T) = a_1 fNIRs(T-1) + \sum b_{1,k} EEG(T-1,k) + e_{fNIRs}(T); k = 0:31. \qquad (23)$$

If we were to choose a model order of 4, then the number of parameters in the model, eq.22, would increase to 132. The increased number of parameters may result in size distortion for the Wald test [37]. Wald test for non-causality is also not consistent if we were to down-sample the EEG whether through skip-sampling or a moving average scheme [37]. Ghysels et. al. proposes a test statistic that can be used to assess causality in such a mixed frequency data [37]. Consider the following multiple parsimonious regression models:

$$fNIRs(T) = \sum_{i=1}^{P} a_i^j fNIRs(T-i) + \beta_j EEG(T-j) + e_{fNIRS}^j(T); \quad j = 1:PM. \qquad (24)$$

Ghysels shows that the high-sampled time series is non-causal to the low-frequency time series, if and only if all the coefficients $\beta_j, j = 1:PM$ are zero. Therefore, he proposes to use the MAX test statistic $\tau = \max_{1 \leq j \leq PM} \left(\sqrt{T_L} \beta_j \right)^2$ to test for causality from the high-frequency time series to the low-frequency time series; T_L is the length of the recording of the low-frequency time series. The distribution for τ under the null hypothesis of non-causality is calculated in [37].

3.2.5. Model Order and Window Size Selection

The model order specifies the number of lags that are included in the autoregressive equation, Eq. 24. As the true underlying autoregressive process that generates the data is unknown, the model order is usually selected by using Akaike Information Criteria [17]. I chose my model order high enough such that adding any more lags from the low-frequency data in the autoregressive (AR) model did not change the variance of the residual term. In most cases, after including four lags of the fNIRs recording, the autocorrelation of the residual signal was of the form of a Dirac delta function; this, in turn, suggested that including more lags would not have reduced the residual, see figure 9. Hence I estimated 128 regression models, each including four lags from the fNIRs and a single lag from the EEG.
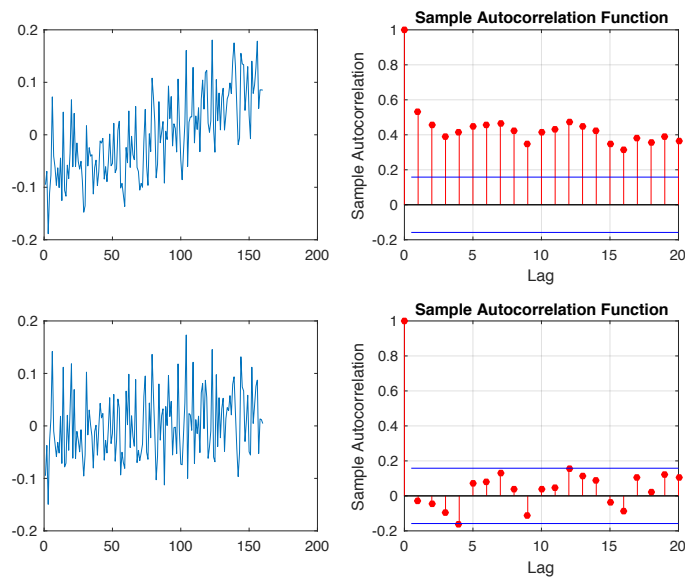
Figure 9.The upper plot shows an fNIRs recording for 20 seconds and its corresponding autocorrelation function. The lower plot shows the residual after including four lags in the AR model; the horizontal lines signify the confidence interval.

In [37], the author suggests to include at least 80 low-frequency data points for estimating the parameters of a model with two lags. As I had included four lags in my model, correspondingly I chose to use a window size of 160 samples, 20 seconds.

3.2.6. EEG Occipital Alpha Rhythm

EEG recordings for O1 and O2 were divided into windows of the length of 2 seconds and the power in the alpha band, 8-12 Hz, in each window was calculated using fast Fourier transform; this amounted to having a frequency resolution of 0.5 Hz. Each window was centered at points corresponding to the time points when fNIRs was sampled. The resulting times series which represented the fluctuation of the alpha power in O1 and O2 electrodes were averaged to calculate the total measured alpha activity in the occipital region.

 HRF was extracted from NIRS_SPM toolbox in MATLAB, shown in the following figure, and was convolved with the calculated alpha activity. The correlation of the resulting waveform and the fNIRs recording was calculated for overlapping windows of 40 seconds; each window overlapped the previous window for 20 seconds.
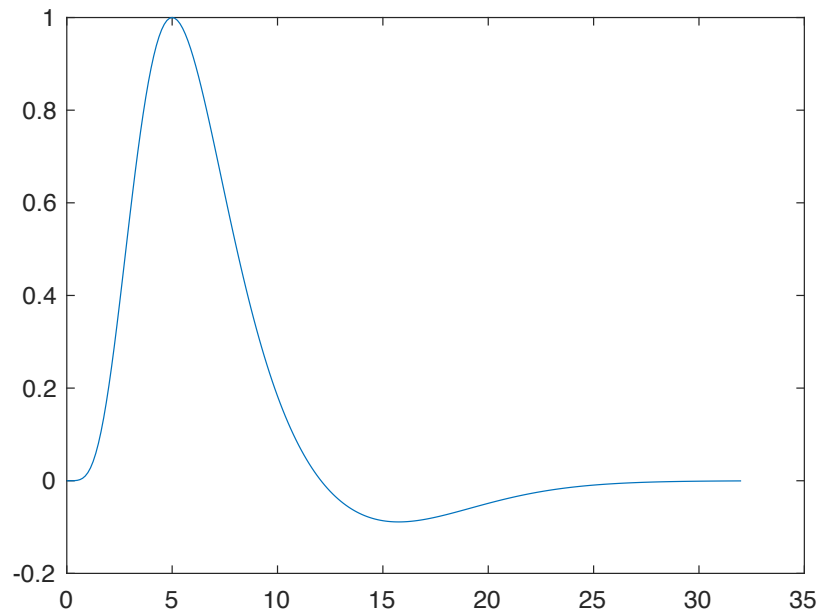
Figure 10.. Hemodynamic Response Function Sampled at 8 Hz. The x-axis shows the times (seconds), and the y-axis shows the amplitude of the HRF. The amplitude was scaled so that the maximum value corresponded to one unit.

3.3. Results

3.3.1. EEG-fNIRs Causality

MAX test statistic for EEG to fNIRs causality was calculated for windows of the length of 20 seconds; each window overlapped the previous window for 19 seconds. The following figure shows the MAX test calculated between EEG and fNIRs recording at electrode Fp1.
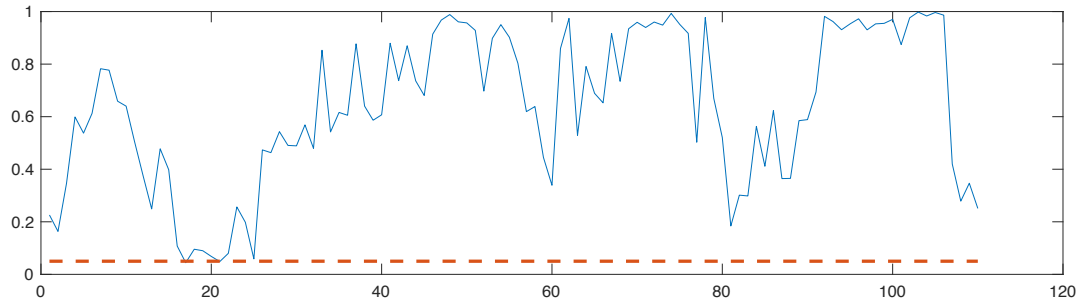
Figure 11.Max test calculated for EEG to fNIRs causality at electrode Fp1 for one subject. The x-axis shows the time (seconds) and the y-axis shows the calculated p-value. The horizontal dashed line depicts the significance level of 0.05.

I then calculated the percentage of time in each recording where MAX test was below the 0.05 significance level; below the dashed line in Figure 11. Following table shows the results for all eight subjects and all the fourteen electrode locations:

Table 2.Percentage of time the hypothesis that EEG is causal to fNIRs was found significant across eight subjects and fourteen electrode locations. Empty positions correspond to electrodes that were rejected due to their high noise.

	S1	S2	S3	S4	S5	S6	S7	S8
'Fp1'	1	7	8	8	5	0	3	1
'F3'	3	16	10	9	12	7	6	5
'F7'	1	5	4	0	5	5	0	---
'C3'	0	7	16	0	5	1	7	---
'T7'	0	0	1	6	17	2	0	0
'O1'	1	6	4	15	0	3	10	21
'Pz'	10	6	5	16	---	14	0	18
'Fp2'	1	0	7	6	9	3	6	0

44

'Fz'	20	0	3	17	0	2	0	0
'F4'	0	4	2	12	9	11	1	0
'F8'	3	1	1		0	8	4	10
'C4'	0	6	4	4	6	6	2	5
'T8'	10	8	4	8	8	1	4	2
'O2'	0	9	2	0	1	3	0	0

These values were averaged across all subjects. The result is shown in the following table

Table 3.Percentage of time the hypothesis that EEG is causal to fNIRs Oxyhemoglobin data was found significant average across 8 subjects.

'Fp1'	4
'F3'	8
'F7'	3
'C3'	5
'T7'	3
'O1'	7
'Pz'	10
'Fp2'	4
'Fz'	5
'F4'	5
'F8'	4
'C4'	4

'T8'	6
'O2'	2

Table 3 shows that the percentage of time wherein the measured electrical activity was found causal to the measured hemodynamic activity. This value is above five percent for only four channels out of the selected fourteen channels. If EEG were in fact causal to fNIRs, I would intuitively expect to find these values to be on average more than 20-30%. In most of the channels, this value is close to five percent, and I find no evidence of causality from EEG to fNIRs.

3.3.2. EEG Occipital Alpha Rhythm

EEG occipital alpha activity was convolved with HRF. The correlation between the resulting waveform and the recorded fNIRs was calculated for windows of the length 40 seconds; each window overlapped the previous window for 20 seconds. The resulting correlation coefficients were averaged across all subjects, using only the windows wherein the p-value was below 0.001. The following figure shows the topography of this averaged correlation value:
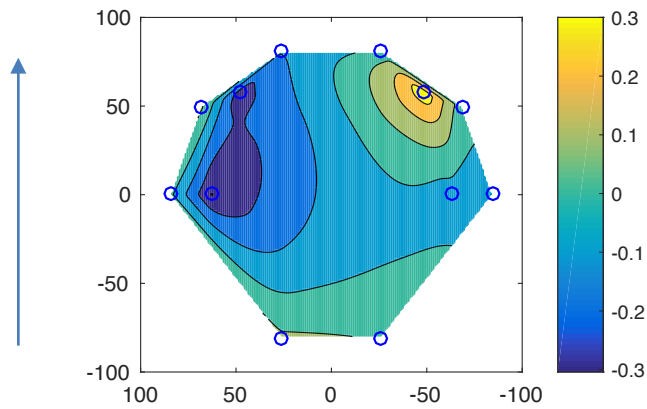
Figure 12.Correlation between Occipital alpha rhythm fluctuation and fNIRs recording at 14 fNIRs channels. The x-axis and the y-axis show the Cartesian BESA coordinate for the electrodes (please see section 2.2.2.1). Circles mark the location of the electrodes. The arrow points toward the anterior part of the head. The colorbar shows the correlation coefficient. How to read the map, the dark blue colored region around F7 has a correlation coefficient of about -0.3 while the yellow region around the electrode F8 has a correlation coefficient of about 0.3.

To investigate if the calculated alpha power was causal to fNIRs, I calculated the MAX test statistic in each window, using sixteen lags (two seconds), and before convolving the alpha power with the HRF. The following table shows the percentage of time the alpha rhythm fluctuations was found causal to fNIRs Oxyhemoglobin changes.

Table 4. Second Column represents percentage of time wherein EEG Occipital Alpha activity was found causal to fNIRs oxyhemoglobin recordings. Third column shows the percentage of time wherein the cross-correlation value of the convolution of EEG Occipital Alpha and HRF with fNIRs was found significant; significance level was set to 0.001

'Fp1'	15	34
'F3'	8	16
'F7'	4	52
'C3'	2	14
'T7'	4	36
'O1'	9	23
'Pz'	10	16
'Fp2'	11	29
'Fz'	3	9
'F4'	6	10

'F8'	6	44
'C4'	5	13
'T8'	6	21
'O2'	12	16

Interestingly, we can observe that for electrodes F8 and F7, while the correlation coefficient was found significant for 52 and 44 percentage of the time, the corresponding causality level was only found significant for only four and six percentage of the time.

3.4. Conclusions

My results in both cases suggest that EEG is not causal to fNIRs. Interestingly, in the case of the alpha fluctuations, despite the significant cross-covariance between these two modalities, causality analysis shows that alpha fluctuations are not causal to fNIRs. I hypothesized that the reason no significant causality was observed from EEG to fNIRs was due to choosing an insufficient model order and not including enough information from the past of the EEG; note that HRF response peak has a latency of 6 seconds. Therefore, I decided to delay EEG recordings by 2.5 and 5.5 seconds in the case of EEG-fNIRs causality and by 4 seconds in the case of Alpha occipital activity and re-do the analysis. However, the results still showed that no causality could be seen between these two modalities:

Table 5. The first two columns, Delay 2.5s and Delay 5.5s, show the percentage of the time where EEG was found causal to fNIRs after delaying the recorded EEG for respectively 2.5 seconds and 5.5 seconds. The last column shows the percentage of the time where occipital alpha activity was found causal to fNIRs after delaying the measured alpha power for 4 seconds.

Electrode	Delay of 2.5 s	Delay of 5.5s	Occipital Alpha 4s delay
'Fp1'	2	1	5
'F3'	7	3	7
'F7'	4	4	9
'C3'	4	10	10
'T7'	5	4	13
'O1'	7	7	9
'Pz'	7	4	6
'Fp2'	6	4	11
'Fz'	13	6	7
'F4'	5	4	14
'F8'	2	8	4
'C4'	4	4	5
'T8'	3	4	11
'O2'	5	3	4

Cross-covariance analysis shows that at electrode sites F8 and F7, about 50% of the recording length, EEG occipital alpha activity has a significance correlation with the recorded fNIRs signal. On the other hand, causality analysis results show that Occipital Alpha activity is not causal to the measured fNIRs signal; see Table 4. This, in turn, rejects any discussion that leads to the conclusion that the alpha rhythm is causing the hemodynamic fluctuations. Furthermore, I was unable to identify any causal relation

between the EEG signals recorded at the chosen electrode site to the observed hemodynamic activity.

Chapter 4

Conclusions And Future Work

A plethora of experimental evidence demonstrates the collaborative and synchronized activity across neural assemblies [1]-[6]. Advances in the multimodal and the multichannel recording of the brain's activity provides us with the opportunity to study this collaboration and synchronization in detail. However, to be able to make use of and to exploit the extensive information that is available through these imaging techniques, one requires advanced signal analysis tools. Tools that will enable him to harness and translate this information into a meaningful characterization of the underlying mechanisms that generates the given data. Causality analysis is one of the tools that allows us to investigate and study the paths of information flow and connectivity in the brain.

In this experimental work, I have used the causality analysis to study the spatial distribution of sources and sinks of information in the brain. My data consisted of five minutes of EEG recording for eight subjects in resting state with the eyes open at 30 electrode sites. Specifically, I have used a simple modification of direct transfer function and Granger's causality to localize the sources and the sinks of information. My results show that in both the theta band (4-8 Hz) and the alpha band (8-12) Hz, the sources of information are localized to the frontal and the occipital areas, see Figures 4 and 5. I found that the frontal areas accounted for about fourteen percent of the total information transmitted across the brain while the occipital region accounts for only 2 percent. On the other hand, I found that the sinks of information have a spatial distribution opposite to

that of the sources. My results show that the sinks of information are localized to the area

bounded by the electrodes C3-C4-FC1-FC2-CP1-CP2 ; see Figure 6 and 7.

I have also examined the relation between the brain's electrical activity measured through

EEG and its hemodynamic activity recorded using fNIRs. My data consisted of five

minutes of EEG recording for eight subjects in resting state with the eyes open at 15

electrode sites. Using a modified version of Granger's causality, applicable to mixed

frequency data, I found no evidence that brain's electrical activity is causing its

hemodynamic activity, see Table 3. I also investigated the relation between the brain's

hemodynamic fluctuations and the spontaneous occipital alpha rhythm. Although my

results show that there is a significant correlation between the occipital alpha rhythm and

the hemodynamic fluctuations at the electrode sites F8 and F7, causality analysis did not

reveal any causal influence from the alpha rhythm to the hemodynamic activity, see

Table 4.

In the first part of this thesis, I had limited my investigation to only thirty electrodes. The

same method of analysis can be applied to investigate the source and the sink maps when

the data has been recorded using 64 electrodes. The increased spatial resolution can help

identify the variations in the source and sink distribution in more detail. Also, given the

new information that is available through the 34 more recording sites, one can expect to

find new paths of information transfer and connectivity. This method can also be applied

to study the variations in connectivity structure of the brain and the source and sink

distribution in the gamma and the beta band.

Increasing the number of electrodes would also help the study of causality between EEG

and fNIRs. The same method that was used in the third chapter can be employed to

investigate the causal interaction between these two modalities with increased spatial distribution.

My results in the second chapter suggest that the sources of information were localized to the frontal region in both the theta band and the alpha band. Hence, it can be very insightful to study the relation between the brain's hemodynamic fluctuations and the spontaneous frontal alpha and theta rhythm.

Refrences

[1]   A. K. Engel, P. Koning, C. M. Gray, and W. Singer, "Stimulus-dependent neuronal oscillations in cat visual cortex: Inter-columnar interaction as determined by cross-correlation analysis," *European Journal of Neuroscience*, vol. 2, no. 7. pp. 588–606, 1990.

[2]   A. K. Engel, P. Konig, A. K. Kreiter, and W. Singer, "Interhemispheric synchronization of oscillatory neuronal responses in cat visual cortex," *Science (80-.).*, vol. 252, no. 5010, pp. 1177–1179, 1991.

[3]   P. R. Roelfsema, A. K. Engel, P. König, and W. Singer, "Visuomotor integration is associated with zero time-lag synchronization among cortical areas.," *Nature*, vol. 385, no. 6612. pp. 157–61, 1997.

[4]   H. Tiitinen, J. Sinkkonen, K. Reinikainen, K. Alho, J. Lavikainen, and R. Naatanen, "Selective attention enhances the auditory 40-Hz transient response in humans," *Nature*, vol. 364, no. 6432, pp. 59–60, 1993.

[5]   P. J. Uhlhaas and W. Singer, "Neural Synchrony in Brain Disorders: Relevance for Cognitive Dysfunctions and Pathophysiology," *Neuron*, vol. 52, no. 1, pp. 155–168, 2006.

[6]   R. W. Thatcher, D. M. North, and C. J. Biver, "Development of cortical connections as measured by EEG coherence and phase delays," *Hum. Brain Mapp.*, vol. 29, no. 12, pp. 1400–1415, 2008.

[7]   T. E. Society, "Investigating Causal Relations by Econometric Models and Cross-spectral Methods Author (s): C . W . J . Granger Published by : The Econometric Society Stable URL : http://www.jstor.org/stable/1912791 Accessed : 26-05-2016 01 : 22 UTC Your use of the JST," vol. 37, no. 3, pp. 424–438, 2016.

[8]   G. Nolte, O. Bai, L. Wheaton, Z. Mari, S. Vorbach, and M. Hallett, "Identifying true brain interaction from EEG data using the imaginary part of coherency," *Clin. Neurophysiol.*, vol. 115, no. 10, pp. 2292–2307, 2004.

[9]   R. Kuś, M. Kamiński, and K. J. Blinowska, "Determination of EEG activity propagation: Pair-wise versus multichannel estimate," *IEEE Trans. Biomed. Eng.*, vol. 51, no. 9, pp. 1501–1510, 2004.

[10]   J. Geweke, "Measurement of Linear Dependence and Feedback between Multiple Time Series," *J. Am. Stat. Assoc.*, vol. 77, no. 378, pp. 304–313, 1982.

[11]   T. J. Ulrych and T. N. Bishop, "Maximum entropy spectral analysis and autoregressive decomposition," *Reviews of Geophysics*, vol. 13. pp. 183–200, 1975.

[12]   A. 1976. Nuttall, "Multivariate linear predictive spectral analysis employing weighted forward and backward averaging: A generalization of Burg's algorithm.," *Nav. Underw. Syst. Cent. NEW LONDON CT*, vol. No. NUSC-T, no. October, 1976.

[13]   J. Makhoul, "Linear Prediction: A Tutorial Review," *Proc. IEEE*, vol. 63, no. 4, pp. 561–580, 1975.

[14]   M. Kamiński, M. Ding, W. a. Truccolo, and S. L. Bressler, "Evaluating causal relations in neural systems: Granger causality, directed transfer function and statistical assessment of significance," *Biol. Cybern.*, vol. 85, no. 2, pp. 145–157, 2001.

[15]   A. Delorme and S. Makeig, "EEGLAB: An open source toolbox for analysis of single-trial EEG dynamics including independent component analysis," *J. Neurosci. Methods*, vol. 134, no. 1, pp. 9–21, 2004.

[16] M. Ding, S. L. Bressler, W. Yang, and H. Liang, "Short-window spectral analysis of cortical event-related potentials by adaptive multivariate autoregressive modeling: data preprocessing, model validation, and variability assessment.," *Biol. Cybern.*, vol. 83, no. 1, pp. 35–45, 2000.

[17] H. Akaike, "A New Look at the Statistical Model Identification," *Autom. Control. IEEE Trans.*, vol. 19, no. 6, pp. 716–723, 1974.

[18] B. He, Y. Dai, L. Astolfi, F. Babiloni, H. Yuan, and L. Yang, "EConnectome: A MATLAB toolbox for mapping and imaging of brain functional connectivity," *J. Neurosci. Methods*, vol. 195, no. 2, pp. 261–269, 2011.

[19] P. S. and R. Moses, *Spectral Analysis of Signals*. 2004.

[20] R. J. Barry, A. R. Clarke, S. J. Johnstone, and C. R. Brown, "EEG differences in children between eyes-closed and eyes-open resting conditions," *Clin. Neurophysiol.*, vol. 120, no. 10, pp. 1806–1811, 2009.

[21] R. D. Pascual-Marqui, R. J. Biscay, J. Bosch-Bayard, D. Lehmann, K. Kochi, T. Kinoshita, N. Yamada, and N. Sadato, "Assessing direct paths of intracortical causal information flow of oscillatory activity with the isolated effective coherence (iCoh).," *Front. Hum. Neurosci.*, vol. 8, no. June, p. 448, 2014.

[22] A. Hillebrand, P. Tewarie, E. van Dellen, M. Yu, E. W. S. Carbo, L. Douw, A. a Gouw, E. C. W. van Straaten, and C. J. Stam, "Direction of information flow in large-scale resting-state networks is frequency-dependent.," *1*, vol. 113, no. 14, pp. 3867–3872, 2016.

[23] K. J. Blinowska, R. Kuś, and M. Kamiński, "Granger causality and information flow in multivariate processes," *Phys. Rev. E - Stat. Nonlinear, Soft Matter Phys.*, vol. 70, no. 5 1, pp. 1–4, 2004.

[24] J. Ito, A. R. Nikolaev, and C. Van Leeuwen, "Spatial and temporal structure of phase synchronization of spontaneous alpha EEG activity," *Biol. Cybern.*, vol. 92, no. 1, pp. 54–60, 2005.

[25] G. Nolte, A. Ziehe, V. V. Nikulin, A. Schl??gl, N. Kr??mer, T. Brismar, and K. R. M??ller, "Robustly estimating the flow direction of information in complex physical systems," *Phys. Rev. Lett.*, vol. 100, no. 23, pp. 1–4, 2008.

[26] T. Inouye, K. Shinosaki, and A. Yagasaki, "The direction of spread of alpha activity over the scalp," *Electroencephalogr. Clin. Neurophysiol.*, vol. 55, no. 3, pp. 290–300, 1983.

[27] M. Jones, J. Berwick, D. Johnston, and J. Mayhew, "Concurrent optical imaging spectroscopy and laser-Doppler flowmetry: the relationship between blood flow, oxygenation, and volume in rodent barrel cortex.," *Neuroimage*, vol. 13, no. 6 Pt 1, pp. 1002–15, 2001.

[28] K. Caesar, L. Gold, and M. Lauritzen, "Context sensitivity of activity-dependent increases in cerebral blood flow.," *Proc. Natl. Acad. Sci. U. S. A.*, vol. 100, no. 7, pp. 4239–4244, 2003.

[29] C. Martin, J. Martindale, J. Berwick, and J. Mayhew, "Investigating neural-hemodynamic coupling and the hemodynamic response function in the awake rat," *Neuroimage*, vol. 32, no. 1, pp. 33–48, 2006.

[30] N. K. Logothetis, "The underpinnings of the BOLD functional magnetic resonance imaging signal.," *J. Neurosci.*, vol. 23, no. 10, pp. 3963–3971, 2003.

[31] N. K. Logothetis, "The neural basis of the blood-oxygen-level-dependent functional magnetic resonance imaging signal," *Philos. Trans. R. Soc. B Biol. Sci.*, vol. 357, no. 1424, pp. 1003–1037, 2002.

[32] M. Cohen, "Parametric Analysis of fMRI Data Using Linear Systems Methods," *Neuroimage*, vol. 6, no. 2, pp. 93–103, 1997.

[33]   R. I. Goldman, J. M. Stern, J. Engel, and M. S. Cohen, "Simultaneous EEG and fMRI of the alpha rhythm.," *Neuroreport*, vol. 13, no. 18, pp. 2487–92, 2002.

[34]   H. Laufs, J. L. Holt, R. Elfont, M. Krams, J. S. Paul, K. Krakow, and A. Kleinschmidt, "Where the BOLD signal goes when alpha EEG leaves," *Neuroimage*, vol. 31, no. 4, pp. 1408–1418, 2006.

[35]   H. Laufs, A. Kleinschmidt, A. Beyerle, E. Eger, A. Salek-Haddadi, C. Preibisch, and K. Krakow, "EEG-correlated fMRI of human alpha activity," *Neuroimage*, vol. 19, no. 4, pp. 1463–1476, 2003.

[36]   P. L. Nunez, B. M. Wingeier, and R. B. Silberstein, "Spatial-Temporal Structures of Human Alpha Rhythms : Theory , Microcurrent Sources , Multiscale Measurements , and Global Binding of Local Networks," vol. 164, pp. 125–164, 2001.

[37]   E. Ghysels and J. B. Hill, "Simple Granger Causality Tests for Mixed Frequency Data," *Work. Pap.*, 2015.

Biographical information

Borzou Alipourfard was born in Tehran, Iran on March 16th, 1993. He completed his Bachelors in biomedical engineering at the AmirKabir University of Technology, Iran in August 2014. In the Spring of 2015, he began his graduate studies at University of Texas at Arlington in Biomedical Engineering. His research work during the graduate course involved EEG signal analysis. He is now pursuing his interests in data analysis by continuing his academic career towards a Ph.D. degree at the Computer Science department of the University of Texas at Arlington under the supervision of Dr. Jean X. Gao.